Generalized Head Models for MEG/EEG: BEM beyond Nested Volumes

Jan Kybic*, Maureen Clerc+, Olivier Faugeras, Renaud Keriven+, Théo Papadopoulo

Odyssée Laboratory – ENPC/ENS/INRIA. Address: INRIA, 2004 Route des Lucioles, BP93, 06902 Sophia-Antipolis, France.
*Center for Machine Perception, Faculty of Electrical Engineering, Czech Technical University in Prague, Czech Republic.
+CERTIS, Ecole Nationale des Ponts et Chaussées, France.

E-mail: kybic@fel.cvut.cz, Maureen.Clerc@sophia.inria.fr

Abstract. Accurate geometrical models of the head are necessary for solving the forward and inverse problems of magneto- and electro-encephalography (MEG/EEG). Boundary element methods (BEM) require a geometrical model describing the interfaces between different tissue types. Classically, head models with a nested volume topology have been used. In this manuscript, we demonstrate how this constraint can be relaxed, allowing to model more realistic head topologies. We describe the symmetric BEM for this new model. The symmetric BEM formulation uses both potentials and currents on the interfaces as unknowns and is in general more accurate than the alternative double-layer formulation.

PACS numbers: 41.20.Cv

Submitted to: *Physics in Medicine and Biology*

1. Introduction

Magneto/electro-encephalography [1–3] is a non-invasive medical technique for measuring neuronal activity in the brain. A classical approach to computing the dependences between the neuronal sources and the electric and magnetic field measured outside the head is the boundary element method (BEM) [4, 5]. A symmetric BEM formulation [6, 7] was demonstrated to be much more accurate than the previously used alternatives, mainly based on the double-layer formulation [8]. The problem we address in this paper is the limitation of the classically used head models consisting of a set of nested closed surfaces. Nested models fail to model the openings present in the skull (eyes), or the brain and skull defects caused by surgery. The effect of such defects on the localization accuracy can be significant [9, 10]. We therefore propose a new formulation that can handle arbitrary partitioning of the space into volumes corresponding to different tissue types.

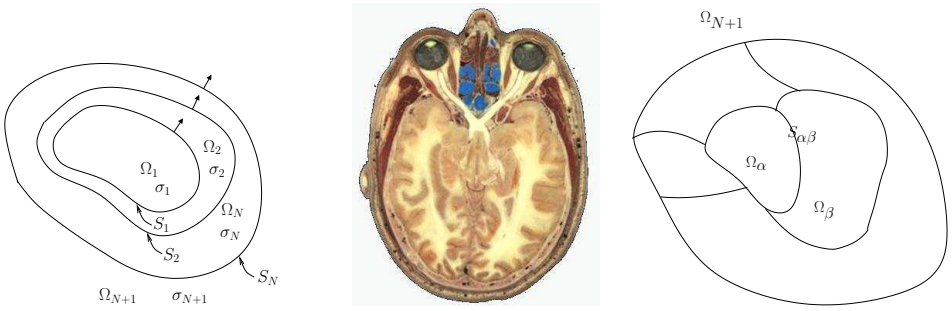

Figure 1. Traditionally, the head is modeled as a set of nested regions (left), while a real head geometry is much more complex (middle, transversal cut from the Visible Human project). The model proposed here assumes piecewise constant conductivity, with arbitrary partitioning (right).

1.1. Problem definition

The relationship between the current source density $\mathbf{J}^p$ and the electric potential V in a conducting environment is given by the quasi-static approximation of Maxwell equations [2, 11]

$$\nabla \cdot \big(\sigma \nabla V\big) = f = \nabla \cdot \mathbf{J}^p \quad \text{in } \mathbb{R}^3 \ . \tag{1}$$

The forward problem consists of calculating V given $\mathbf{J}^p$ and σ. We only consider piecewise constant conductivity models, with different conductivities corresponding to different tissue types. Such models can be constructed readily (although laboriously) from segmented MRI data.

1.2. Previous work

Previous BEM models for MEG/EEG [1, 7, 12–15] have been limited to simple nested models (Figure 1, left). However, it is clear that an actual head geometry (Figure 1, middle) is topologically more intricate. For example, nested models cannot represent the openings present in the skull (eyes). We propose a new formulation that can handle arbitrary partitioning of the space into volumes corresponding to different tissue types.

The importance of using head models with a general topology is becoming apparent. It was proved for example that ignoring a hole in the skull can cause localization errors of up to 2 cm [9]. The standard BEM, capable of handling closed surfaces, was applied to this case [10] by using meshes composed of closed surfaces approximating the true, general topology. This was done either by describing the inner and outer skull surfaces by a single interface, by making different meshes partly coincide, or by introducing an infinitely thin skull layer surrounding the compartment representing the hole. Unfortunately, bringing surfaces close together deteriorates the numerical accuracy of the BEM.

The classical double-layer BEM has been applied to a general topology in [16], without justification of the validity of this extension. An isolated problem approach [15] was used to mitigate the numerical inaccuracy of the double-layer BEM for large conductivity differences.

1.3. Generalized head model

We consider a head model with piecewise-constant conductivity, by partitioning the space into $N+1$ disjoint connected open sets $\Omega_1, \ldots, \Omega_{N+1}$, such that $\bigcup_{\alpha=1}^{N} \overline{\Omega}_\alpha \cup \Omega_{N+1} = \mathbb{R}^3$. The volumes $\Omega_1, \ldots, \Omega_N$, with conductivities σ_α, correspond to head tissues and are bounded, while Ω_{N+1}, with conductivity $\sigma_{N+1} = 0$, represents the air and extends to infinity (Figure 1, right)

Each pair of volumes $\Omega_\alpha, \Omega_\beta$ has a common boundary $S_{\alpha\beta} = \partial\Omega_\alpha \cap \partial\Omega_\beta$ which is either empty, or can be decomposed as the union of a finite number of connected regular surfaces‡. Note that each $S_{\alpha\beta}$ is regular almost everywhere, and has a normal field $\mathbf{n}$ which points, by definition, from Ω_α to Ω_β.

1.4. Connected Laplace problems

Since the conductivity is supposed to be piecewise constant, we can factor out σ from (1) to yield a set of Laplace problems connected by boundary conditions, imposing the continuity of potential V and current $p = \sigma\partial_{\mathbf{n}} V$ across the interfaces:

$$\sigma_\alpha \Delta V = f \quad \text{in all } \Omega_\alpha \tag{2}$$

$$\big[V\big]_{S_{\alpha\beta}} = \big[p\big]_{S_{\alpha\beta}} = 0 \quad \text{on all } S_{\alpha\beta}\ . \tag{3}$$

2. Symmetric Boundary Element Method

The symmetric boundary element method (BEM) [5] uses Green identities to convert the differential equations (2) for V in $\mathbb{R}^3$ into a set of integral equations with unknowns V and p on the boundaries $S_{\alpha\beta}$, reducing the dimensionality of the problem from 3D to 2D. A discretization leads to a symmetric system of linear equations. The symmetric BEM formulation is more complicated but more accurate and numerically stable than the alternative double-layer and single-layer BEM [17]. Originally, the symmetric BEM was formulated for the layered model [7]. We shall go over it again briefly, making the appropriate changes to allow for the generalized head model (Section 1.3), as already hinted in [18].

2.1. Free-space solution

Let us first consider a solution of (2) without taking the boundary conditions (3) into account, as if it were in an infinite space of constant conductivity. Let us decompose the sources as $f = \sum_\alpha f_\alpha$, such that for each α and for all $\mathbf{x} \notin \Omega_\alpha$, $f_\alpha(\mathbf{x}) = 0$. For α such that $\sigma_\alpha \neq 0$, we denote by v_α a free-space solution of

$$\sigma_\alpha \Delta v_\alpha = f_\alpha\ . \tag{4}$$

We introduce the Green function $G(\mathbf{r}) = 1/\big(4\pi\|\mathbf{r}\|\big)$ of the Laplace operator, such that $-\Delta G(\mathbf{r}) = \delta_0(\mathbf{r})$. The function $v_\alpha = -\big(f_\alpha * G\big)/\sigma_\alpha$ satisfies (4). This free space solution v_α also satisfies the "zero at infinity" condition (denoted $\mathscr{H}$ in the Representation Theorem, Appendix 2), which ensures that v_α tends to zero infinitely far from all sources.

In volumes such as Ω_{N+1} (air), where the conductivity $\sigma_{N+1} = 0$, we choose $v_{N+1} = 0$, a valid solution of (4) which is also compatible with the condition $\mathscr{H}$.

‡ A surface S is connected if for each pair of points $A, B \in S$ there is a path in S between A and B. A surface is regular if at each point it can be locally approximated by a plane.

2.2. Continuous form of the symmetric BEM

Let us now describe how to convert the partial differential equations (2), and boundary conditions (3) into the integral formulation. In each Ω_α, we define a function

$$u_\alpha = \begin{cases} V - v_\alpha & \text{in } \Omega_\alpha \\ -v_\alpha & \text{elsewhere,} \end{cases}$$

where V is the solution of equations (2,3) and v_α the solution of (4). The function u_α is harmonic ($\Delta u_\alpha = 0$) in $\mathbb{R}^3 \backslash \partial\Omega_\alpha$. It jumps across the boundary $\partial\Omega_\alpha$ (between Ω_α and $\mathbb{R}^3 \backslash \Omega_\alpha$) according to $[u_\alpha]_{\partial\Omega_\alpha} = V_\alpha$ and $\sigma_\alpha [\partial_{\mathbf{n}} u_\alpha]_{\partial\Omega_\alpha} \stackrel{\text{def}}{=} p_\alpha$, where V_α is the restriction of V on the boundary. (The jump of f between Ω_α and Ω_β is defined as $[f]_{S_{\alpha\beta}} = f^\alpha_{S_{\alpha\beta}} - f^\beta_{S_{\alpha\beta}}$, where $f^\alpha_{S_{\alpha\beta}}$, resp. $f^\beta_{S_{\alpha\beta}}$, are the limits of f when approaching a point on the surface $S_{\alpha\beta}$ from Ω_α, resp. Ω_β.)

Consider the surface $S_{\alpha\beta} = \Gamma$. First, we apply the Representation Theorem [4, 5] (Appendix 2) to calculate the limit of $u_\alpha = V - v_\alpha$ from Ω_α towards Γ, using the values of V and p on all the boundary $\partial\Omega_\alpha$, $\Gamma \subseteq \partial\Omega_\alpha$:

$$\begin{aligned} \big(V - v_\alpha\big)^-_\Gamma &= \frac{[u_\alpha]_\Gamma}{2} - \sum_{\Theta = S_{\alpha\delta}} \big(\mathcal{D}_{\Gamma\Theta}\big[u_\alpha\big]_\Theta - \mathcal{S}_{\Gamma\Theta}\big[\partial_{\mathbf{n}} u_\alpha\big]_\Theta\big) \\ &= \frac{V_\Gamma}{2} - \sum_{\Theta = S_{\alpha\delta}} \big(\mathcal{D}_{\Gamma\Theta} V_\Theta - \sigma_\alpha^{-1} \mathcal{S}_{\Gamma\Theta} p_\Theta\big) \end{aligned}$$

where $\mathcal{D}$ and $\mathcal{S}$ are the double- resp. single-layer potential integral operators [7, 17] (see also Appendix 1), the subscripts indicate the target and source surfaces they operate upon, and we sum over all regions Ω_δ adjacent to Ω_α. Second, we apply the Representation Theorem to the limit of $u_\beta = V - v_\beta$ from Ω_β towards Γ:

$$\begin{aligned} \big(V - v_\beta\big)^+_\Gamma &= -\frac{[u_\beta]_\Gamma}{2} + \sum_{\Theta = S_{\beta\delta}} \big(-\mathcal{D}_{\Gamma\Theta}\big[u_\beta\big]_\Theta - \mathcal{S}_{\Gamma\Theta}\big[\partial_{\mathbf{n}} u_\beta\big]_\Theta\big) \\ &= \frac{V_\Gamma}{2} + \sum_{\Theta = S_{\beta\delta}} \Big(\mathcal{D}_{\Gamma\Theta} V_\Theta - \sigma_\beta^{-1} \mathcal{S}_{\Gamma\Theta} p_\Theta\Big) \end{aligned}$$

where the "inward" orientation of Γ with respect to Ω_β changes the sign of the normal derivative $\partial_{\mathbf{n}}$ involved in $\mathcal{D}$ and p. Thanks to the continuity of v_α,v_β, and V across Γ we can subtract the two previous equations:

$$\big(v_\beta - v_\alpha\big)_\Gamma = -2\mathcal{D}_{\Gamma\Gamma} V_\Gamma + (\sigma_\beta^{-1} + \sigma_\alpha^{-1}) \mathcal{S}_{\Gamma\Gamma} p_\Gamma - \sum_{(\Theta,\gamma)} \big(\mathcal{D}_{\Gamma\Theta} V_\Theta - \sigma_\gamma^{-1} \mathcal{S}_{\Gamma\Theta} p_\Theta\big) \tag{5}$$

with $(\Theta, \gamma) \in \big\{(S_{\alpha\delta}, \alpha); \delta \neq \beta\big\} \cup \big\{(S_{\delta\beta}, \beta); \delta \neq \alpha\big\}$. Similarly, by evaluating $\big(\sigma \partial_{\mathbf{n}} u\big)$ on both sides of Γ we get:

$$\begin{aligned} &\big(\sigma_\beta \partial_{\mathbf{n}} v_\beta - \sigma_\alpha \partial_{\mathbf{n}} v_\alpha\big)_\Gamma = \\ &\qquad -(\sigma_\alpha + \sigma_\beta) \mathcal{N}_{\Gamma\Gamma} V_\Gamma + 2\mathcal{D}^*_{\Gamma\Gamma} p_\Gamma - \sum_{(\Theta,\gamma)} (\sigma_\gamma \mathcal{N}_{\Gamma\Theta} V_\Theta - \mathcal{D}^*_{\Gamma\Theta} p_\Theta) \end{aligned} \tag{6}$$

with the same (Θ, γ). We have obtained a set of equations for V and p that must hold on all surfaces. Note that, since $\sigma_{N+1} = 0$, the flow p across the external surfaces is 0, and the corresponding terms disappear.

2.3. Discretization of unknowns and surfaces

The surfaces $S_{\alpha\beta}$ are triangulated, and the vertices common to several surfaces are shared. To balance approximation errors, the potential V is discretized on the surfaces using piecewise linear P1 elements $\{\varphi_k\}$ (with k indexing the vertices of the triangulated surfaces) and the flow p using the piecewise constant P0 elements $\{\psi_l\}$ (with l indexing the triangles of the triangulated surfaces), like in [7]. Unlike the ψ_l, the P1 functions φ_k span several triangles which can belong to different surfaces. We therefore decompose them as $\varphi_k = \sum_{k'(k)} \varphi'_{k'}$, where the notation $k'(k)$ means "the indices k' of triangles that contain the vertex of index k". Each of the partial functions $\varphi'_{k'}$ is supported only on one (oriented) triangle $T_{k'}$ and hence belongs only to one surface. We approximate the unknowns as

$$V = \sum_{k=1}^{N_v} \sum_{k'(k)} x_k \varphi'_{k'} \qquad \text{and} \qquad p = \sum_{l=1}^{N_t} y_l \psi_l \tag{7}$$

where N_v, resp. N_t are the total numbers of vertices, resp. triangles, across all surfaces.

2.4. Discretization of the equations

Using a Galerkin approach, we take scalar products of both sides of (6) with P1 basis functions φ_i and of both sides of (5) with P0 basis functions ψ_j, on $S_{\alpha\beta} = \Gamma$:

$$\underbrace{\big\langle (\sigma_\beta \partial_{\mathbf{n}} v_\beta - \sigma_\alpha \partial_{\mathbf{n}} v_\alpha), \varphi_i \big\rangle}_{w_i} = \sum_{i'(i)} \Big(\sum_k x_k \sum_{k'(k)} \delta_{i'k'} \big(\mathsf{N}\big)_{i'k'} + \sum_l y_l \mu_{i'l} \big(\mathsf{D}^*\big)_{i'l} \Big) \tag{8}$$

$$\underbrace{\big\langle (v_\beta - v_\alpha), \psi_j \big\rangle}_{z_j} = \sum_k x_k \sum_{k'(k)} \mu_{jk'} \big(\mathsf{D}\big)_{jk'} + \sum_l y_l \nu_{jl} \big(\mathsf{S}\big)_{jl} \ . \tag{9}$$

The discretized operator matrices are

$$\begin{aligned} \big(\mathsf{N}\big)_{i'k'} &= \big\langle \mathcal{N}_{\Gamma\Theta} \varphi'_{k'}, \varphi'_{i'} \big\rangle \\ \big(\mathsf{S}\big)_{jl} &= \big\langle \mathcal{S}_{\Gamma\Theta} \psi_l, \psi_j \big\rangle \\ \big(\mathsf{D}\big)_{jk'} &= \big(\mathsf{D}^*\big)_{k'j} = \big\langle \mathcal{D}_{\Gamma\Theta} \varphi'_{k'}, \psi_j \big\rangle = \big\langle \mathcal{D}^*_{\Theta\Gamma} \psi_j, \varphi'_{k'} \big\rangle, \end{aligned}$$

where φ_i, ψ_j are defined on the surface $\Theta = S_{\gamma\delta}$ or $S_{\delta\gamma}$, $\gamma \in \{\alpha, \beta\}$, Ω_δ adjacent to Ω_γ and the constants are given by §:

$\delta_{i'k'}$	$\mu_{i'l}$	ν_{jl}	condition
$-(\sigma_\alpha + \sigma_\beta)$	-2	$(\sigma_\alpha^{-1} + \sigma_\beta^{-1})$	$\Theta = S_{\alpha\beta}$
$+\sigma_\alpha$	-1	$+\sigma_\alpha^{-1}$	$\Theta = S_{\alpha\delta}, \delta \neq \beta$
$-\sigma_\alpha$	1	$-\sigma_\alpha^{-1}$	$\Theta = S_{\delta\alpha}, \delta \neq \beta$
$+\sigma_\beta$	-1	$+\sigma_\beta^{-1}$	$\Theta = S_{\delta\beta}, \delta \neq \alpha$
$-\sigma_\beta$	1	$-\sigma_\beta^{-1}$	$\Theta = S_{\beta\delta}, \delta \neq \alpha$
0	0	0	otherwise

The advantage of this discretization is a good balance of the regularity of the integrated terms. The system matrix A (composed of N, D, D^*, S, see (10)) is symmetric, provided that we order the equations as written above, (8), (9) and the unknowns as in $\mathsf{A}\,[\mathbf{x}\ \mathbf{y}]^T$.

§ In the first line, Θ is equal to Γ but also to the other components of $\partial\Omega_\alpha \cap \partial\Omega_\beta$, if this boundary is composed of several regular surfaces. Then each coefficient δ, μ, ν is a sum of the individual contributions.

The double integrals involved in evaluating the elements of matrices D^*, D, S are computed partly analytically [12, 19, 20]; the outer integrals are computed numerically using a 16-point triangle quadrature rule [21]. Elements of the LHS of (8,9) are calculated by an adaptive numerical quadrature using the Cubpack++ library [22].

The discretized operator N is approximated using the relation ([5],Theorem 3.3.2):

$$\big\langle \mathcal{N}\varphi'_{i'}, \varphi'_{j'} \big\rangle = -(\mathbf{q}_{i'} \times \mathbf{n}_i) \cdot (\mathbf{q}_{j'} \times \mathbf{n}_j) \big\langle \mathcal{S}\psi_{j'}, \psi_{i'} \big\rangle$$

where the partial P1 basis functions $\varphi_{i'}(\mathbf{x}) = \big(\mathbf{q}_{i'} \cdot \mathbf{x} + \alpha_{i'}\big)\psi_{i'}(\mathbf{x})$ and $\varphi_{j'}(\mathbf{x}) = \big(\mathbf{q}_{j'} \cdot \mathbf{x} + \alpha_{j'}\big)\psi_{j'}(\mathbf{x})$ are supported only on triangles i' resp. j' with normals $\mathbf{n}_{i'}$,$\mathbf{n}_{j'}$.

2.4.1. Three nested layers. As an example, suppose the head model to consist of three nested layers, denoted $1, 2, 3$. The system (8), (9) writes

$$\underbrace{\begin{pmatrix} (\sigma_1+\sigma_2)\mathsf{N}_{11} & -\sigma_2\mathsf{N}_{12} & 0 & -2\mathsf{D}^*_{11} & \mathsf{D}^*_{12} \\ -\sigma_2\mathsf{N}_{21} & (\sigma_2+\sigma_3)\mathsf{N}_{22} & -\sigma_3\mathsf{N}_{23} & \mathsf{D}^*_{21} & -2\mathsf{D}^*_{22} \\ 0 & -\sigma_3\mathsf{N}_{32} & \sigma_3\mathsf{N}_{33} & 0 & \mathsf{D}^*_{32} \\ -2\mathsf{D}_{11} & \mathsf{D}_{12} & 0 & (\sigma_1^{-1}+\sigma_2^{-1})\mathsf{S}_{11} & -\sigma_2^{-1}\mathsf{S}_{12} \\ \mathsf{D}_{21} & -2\mathsf{D}_{22} & \mathsf{D}_{23} & -\sigma_2^{-1}\mathsf{S}_{21} & (\sigma_1^{-1}+\sigma_2^{-1})\mathsf{S}_{22} \end{pmatrix}}_{\mathsf{A}} \cdot \underbrace{\begin{pmatrix} \mathbf{x}_1 \\ \mathbf{x}_2 \\ \mathbf{x}_3 \\ \mathbf{y}_1 \\ \mathbf{y}_2 \end{pmatrix}}_{\mathbf{u}} = \underbrace{\begin{pmatrix} \mathbf{w}_1 \\ \mathbf{w}_2 \\ \mathbf{w}_3 \\ \mathbf{z}_1 \\ \mathbf{z}_2 \end{pmatrix}}_{\mathbf{c}}$$

where $\mathbf{x}_\alpha$, $\mathbf{y}_\alpha$ are the unknown terms from (7) corresponding to the surface α. Similarly, $\mathbf{w}_\alpha$, $\mathbf{z}_\alpha$ are the corresponding source terms from (8), (9).

The zero blocks come from the fact that layers 1 and 3 do not touch a common volume and thus do not interact. If more nested layers are added, it can easily be seen that the system always keeps the structure:

$$\underbrace{\begin{pmatrix} \mathsf{N} & \mathsf{D}^* \\ \mathsf{D} & \mathsf{S} \end{pmatrix}}_{\mathsf{A}} \underbrace{\begin{pmatrix} \mathbf{x} \\ \mathbf{y} \end{pmatrix}}_{\mathbf{u}} = \underbrace{\begin{pmatrix} \mathbf{w} \\ \mathbf{z} \end{pmatrix}}_{\mathbf{c}} \qquad \text{with } \mathsf{D}^* = \mathsf{D}^T. \tag{10}$$

The system is symmetric and the matrices N, D and S are block diagonal (provided a proper ordering of the surfaces has been chosen). Note also that the number of unknowns is less than $N = N_v + N_t$, because since $\sigma_4 = 0$ the system does not depend on $\mathbf{y}_3$.

2.4.2. General topology. If the topology is more general, we can no longer uniquely identify vertex unknowns with surfaces. The overall four-block structure of A remains as in (10) but the block-diagonal structure is lost.

For example, consider the model in Figure 2, consisting of two half-spheres S_a and S_b with the same radius, enclosing volumes with conductivities σ_1 and σ_2, connected together along a disk S_c and included within a larger sphere S_d enclosing a volume with conductivity σ_3, itself placed in a non-conductive medium. In this case, the submatrices have the following structure:

$$\mathsf{N} = \begin{pmatrix} (\sigma_1+\sigma_3)\mathsf{N}_{aa} & -\sigma_3\mathsf{N}_{ab} & -\sigma_1\mathsf{N}_{ac} & -\sigma_3\mathsf{N}_{ad} \\ -\sigma_3\mathsf{N}_{ba} & (\sigma_2+\sigma_3)\mathsf{N}_{bb} & -\sigma_2\mathsf{N}_{bc} & -\sigma_3\mathsf{N}_{bd} \\ -\sigma_1\mathsf{N}_{ca} & -\sigma_2\mathsf{N}_{cb} & (\sigma_1+\sigma_2)\mathsf{N}_{cc} & 0 \\ -\sigma_3\mathsf{N}_{da} & -\sigma_3\mathsf{N}_{db} & 0 & \sigma_3\mathsf{N}_{dd} \end{pmatrix}$$

$$\mathsf{D} = \begin{pmatrix} -2\mathsf{D}_{aa} & \mathsf{D}_{ab} & \mathsf{D}_{ac} & \mathsf{D}_{ad} \\ \mathsf{D}_{ba} & -2\mathsf{D}_{bb} & \mathsf{D}_{bc} & \mathsf{D}_{bd} \\ \mathsf{D}_{ca} & \mathsf{D}_{cb} & -2\mathsf{D}_{cc} & 0 \end{pmatrix}$$

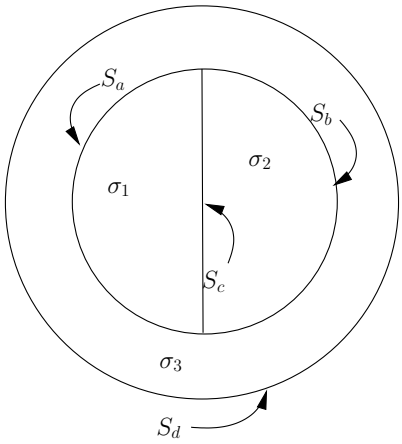

Figure 2. Example of a general, non-nested topology.

and

$$\mathsf{S} = \begin{pmatrix} (\sigma_1^{-1} + \sigma_3^{-1})\mathsf{S}_{aa} & -\sigma_3^{-1}\mathsf{S}_{ab} & -\sigma_1^{-1}\mathsf{S}_{ac} \\ -\sigma_3^{-1}\mathsf{S}_{ba} & (\sigma_2^{-1} + \sigma_3^{-1})\mathsf{S}_{bb} & -\sigma_2^{-1}\mathsf{S}_{bc} \\ -\sigma_1^{-1}\mathsf{S}_{ca} & -\sigma_2^{-1}\mathsf{S}_{cb} & (\sigma_1^{-1} + \sigma_2^{-1})\mathsf{S}_{cc} \end{pmatrix} .$$

The zero blocks in N and D result from the fact that the surfaces S_c and S_d are not the boundaries of a common volume. We can neglect the interaction between S_d and the zero-measure curves at the intersection of S_c and S_a (resp. S_b).

2.5. Deflation and preconditioning

The matrix A as defined in (10) has a kernel of dimension 1, related to the indeterminacy of the absolute level of the potential V. Using deflation [7, 23, 24] we obtain a regular matrix

$$\mathsf{A}' = \mathsf{A} + \omega \mathsf{I}_{\text{defl}}$$

where I_{defl} selects a solution with zero mean of the potential coefficients $\mathbf{x}$ over all the surfaces, i.e. $\mathsf{I}_{\text{defl}}\mathbf{u} = \begin{bmatrix} s & s & \dots & s \end{bmatrix}$ with $s = \sum_i x_i$. In other words, $\mathsf{N}' = \mathsf{N} + \omega \mathbf{1}\mathbf{1}^T$. The constant ω is chosen to approximately maximize the conditioning of A' by equalling the maximum eigenvalues of I_{defl} and an approximation of A by its diagonal elements [7].

The matrix A' is then preconditioned by its diagonal. In other words, instead of solving $\mathsf{A}'\mathbf{u} = \mathbf{c}$, we solve $(\mathsf{D}\mathsf{A}'\mathsf{D})(\mathsf{D}^{-1}\mathbf{u}) = \mathsf{D}\mathbf{c}$, where D is a diagonal matrix such that all diagonal elements of $\mathsf{D}\mathsf{A}'\mathsf{D}$ are equal to 1 in magnitude.

The system matrix A (10) is a so-called saddle-point system [25], indefinite (with both positive and negative eigenvalues) even after the deflation and with relatively poor spectral properties, more difficult to solve than standard positive definite linear systems.

2.6. Iterative solver

The matrix A is big but relatively well structured: since the $\mathcal{N}$, $\mathcal{S}$, $\mathcal{D}$ interactions all decrease with distance between interacting elements, the elements in each block tend

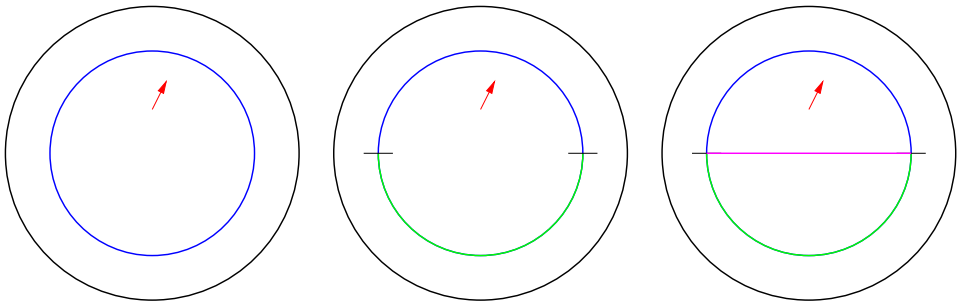

Figure 3. Sketched cross-sections of alternative representations of a two-sphere model: two closed spheres (left), inner sphere divided into two hemispheres (middle), with a separating boundary between the two hemispheres (right).

to get smaller away from the diagonal. Therefore, it is advantageous to use iterative methods for solving $\mathbf{Au} = \mathbf{c}$. We have chosen the MINRES algorithm [26], which is a Krylov subspace method similar to the conjugate gradient method, and designed for symmetric but not necessarily positive-definite matrices. Its convergence speed depends on the eigenstructure of the system matrix [27–29]. Preconditioning reduces the number of iterations by approximately a factor of two.

3. Experiments

We have implemented the generalized topology algorithm presented here using the same core computational routines as in the original symmetric method implementation [7]. We have verified that the matrices corresponding to layered head models are identical to within machine precision.

3.1. Alternative spherical models

The second set of experiments checks the correctness of calculation for more complex topologies, using three equivalent mesh sets. First, we calculated the outside field for a two-layer spherical model with a diagonal, unit-magnitude, dipolar current source. Its cross-section is sketched in Figure 3, left. The conductivities are 1 S/m inside the inner sphere, 0.1 S/m between the inner and outer spheres, and 0 outside. Note that for such a simple model, the EEG forward problem has an analytical solution. The surface electric potential, computed with the BEM for a discretization with 516 points (1024 triangles) per sphere is shown in Figure 4, left. The relative ℓ_2 error with respect to the analytical solution was 3.4 %. Since deflation depends on discretization, mean surface potential was subtracted from all results for meaningful comparison.

In the second case (Figure 3, middle), the inner sphere was divided into two hemispheres. As the system matrix is identical to the first case, the surface field (Figure 4,middle) is also identical to the first case. Finally, we added a dividing surface between the two hemispheres (Figure 3, right), similar to Figure 2, while maintaining the conductivities unchanged. The relative ℓ_2 difference of the potential with respect to the first and second cases was 1.0 %, the error with respect to the analytical solution 3.8 %. These errors are comparable to the error of the BEM itself [7].

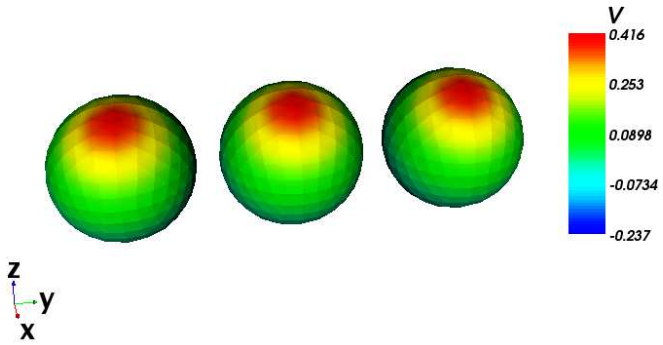

Figure 4. Surface potential for the three alternative representations of the two-sphere model (Figure 3) with 516 to 632 points (1024 to 1280 triangles). Surface potential after mean subtraction is shown. The three results are virtually identical.

3.2. Change of conductivity for spherical models

The third experiment studies the effects of a change of the conductivity of the 'bottom' hemisphere (Figure 3, right) from 10^{-3} to 10^{3}, with the remaining conductivities unchanged (1 for the top hemisphere, 0.1 between the inner and outer spheres). Even though the surface fields look very similar (Figure 5, top), the change is well visible on the graph (Figure 5, bottom) showing the surface potential along a circular intersection of the outer sphere with the zy plane (containing the dipole source) as a function of the angle.

3.3. Refining meshes for a realistic model with a hole

The numerical accuracy can be improved by selectively refining (increasing triangulation density) in regions where abrupt spatial changes of the field are expected.

We created a realistic head model from MRI data with surfaces representing interfaces between the skin ($\sigma = 1$), the skull bone ($\sigma = 0.0125$), and the cerebrospinal fluid (CSF, $\sigma = 1$). The novelty is that we artificially introduced a 'hole' in the skull: a part of the original skull volume now forms an extra compartment, with a separately chosen conductivity σ_{hole}. The hole compartment has common borders with the skull, the brain/CSF and the skin compartments. Such a hole could result from an injury or an operation. We have chosen a realistic dipolar source in the upper half of the innermost compartment, oriented approximately perpendicularly to the skull surface.

We have prepared five variants of this realistic head model (Figure 6): a reference model without the hole (R), a model with coarsely meshed hole walls (A), two models with increasing number of triangle "layers" representing the hole walls (B and C); since the top and bottom surfaces are unchanged, this leads to anisotropic meshes. The last model (D) has the finest hole wall meshing and adaptively refined top and bottom surfaces in the vicinity of the hole, improving the mesh isotropy.

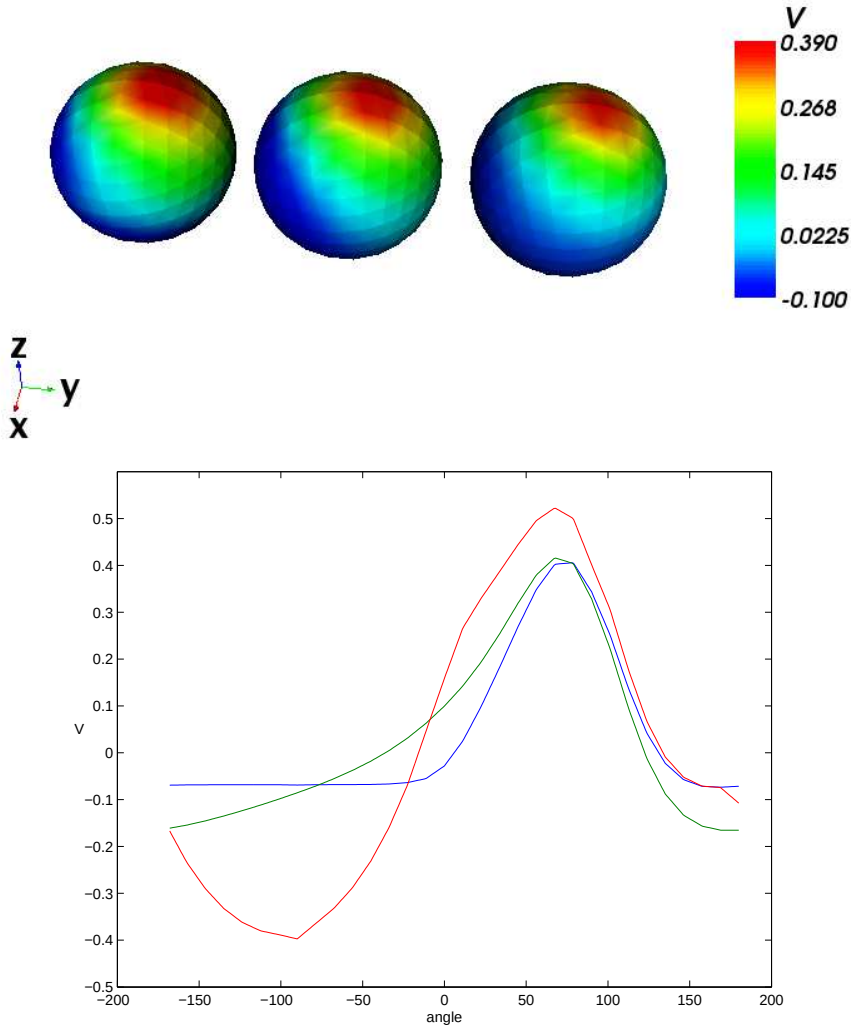

Figure 5. Surface potential for the three-compartment model (Figure 3, right) for conductivities of the bottom hemisphere $\sigma = 10^{-3}, 1, 10^{3}$ (left image — left, middle, right, respectively). Surface potential after mean subtraction is shown. The graph (bottom) shows the potential for the three cconductivities on the surface along an intersection of the outer sphere with the zy plane (containing the dipole source) as a function of the 'elevation' angle. The curve with the highest amplitude corresponds to $\sigma = 10^{-3}$, the middle one to $\sigma = 1$ and the smallest amplitude to $\sigma = 10^{3}$.

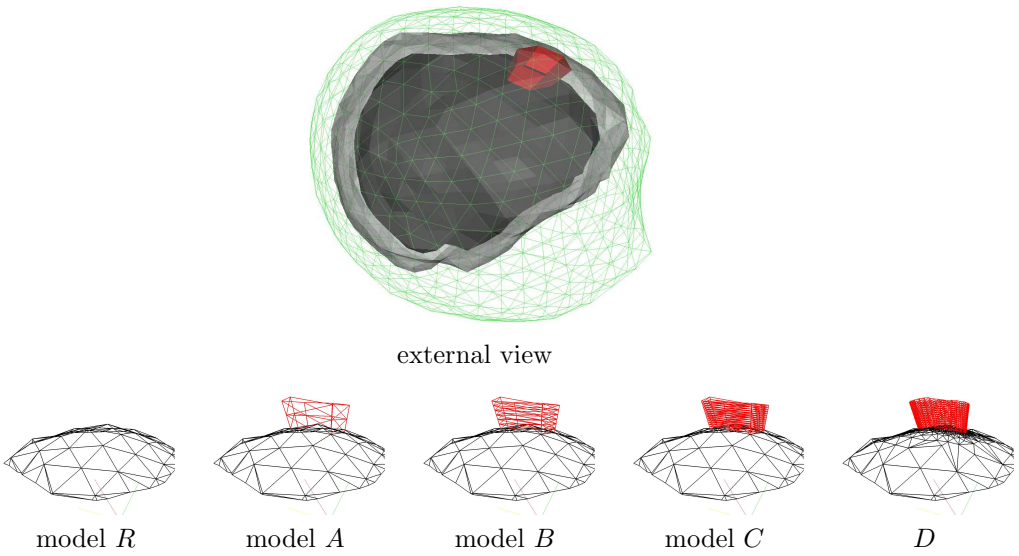

Figure 6. Realistic head models with a hole in the skull. Top: external view. Bottom: close-up view showing the details of the mesh around the hole for models R, A, B, C, D.

The hole conductivity was set equal to that of the bone so that the model without the hole could be used as a reference to assess accuracy. A source dipole was placed in the upper half of the innermost compartment.

The numerical results for the forward problem are reported in Table 1. As expected, the accuracy improves significantly for finer meshes. The condition number of the system matrix‖ remains average in all cases, while the number of MINRES iterations needed grows about linearly with the total number of unknowns. For MINRES, relative residual threshold $\varepsilon = 1e-6$ was used. Double precision LAPACK GESV routine was used for the direct solver.

We observed that reasonably anisotropic, irregular and non-smooth meshes do not deteriorate significantly the numerical accuracy, nor the convergence. However, topological defects — wrong triangle orientation, non-closed surfaces — can have disastrous effects. Similarly, bad geometrical properties – almost but not exactly identical points, or points almost but not quite lying on an edge — can also deteriorate numerical stability of the system. When such a bad quality mesh was used for the same head model as presented here, the MINRES algorithm needed over 10^4 to converge with a relative accuracy of 10^{-2} — this is much worse than the results with a good quality mesh shown in Table 1.

3.4. Changes of conductivity for the realistic model

We have varied the conductivity of the hole compartment of the realistic model (variant D, described above) and observed the changes of the surface field (Figure 7). We found that the changes are significant for a dipole beneath the hole, especially in the case of high conductivity of the hole compartment (corresponding to the hole filled

‖ The null-space of rank 1 was not taken into account since it is taken care of by deflation.

model	N_V	N	σ_1/σ_{N-1}	iterations	residual	error direct	error iter.	time [min]
R	1636	3668	$1.51 \cdot 10^4$	480	$9.11 \cdot 10^{-7}$	—	—	16
A	1642	3698	$1.36 \cdot 10^4$	485	$9.40 \cdot 10^{-7}$	0.93 %	0.97 %	17
B	1666	3770	$1.38 \cdot 10^4$	511	$9.34 \cdot 10^{-7}$	0.82 %	0.96 %	18
C	1714	3914	$1.39 \cdot 10^4$	581	$9.13 \cdot 10^{-7}$	0.60 %	0.92 %	22
D	2921	7613	$1.84 \cdot 10^4$	859	$9.79 \cdot 10^{-7}$	0.19 %	0.41 %	117

Table 1. For head models R, A, B, C, D we show the number of vertices, total number of unknowns, matrix condition number, number of MINRES iterations, relative residual, relative ℓ_2 errors with respect to the reference model R for the MINRES and direct solvers, and approximate processor time (on 2 GHz AMD Opteron processor).

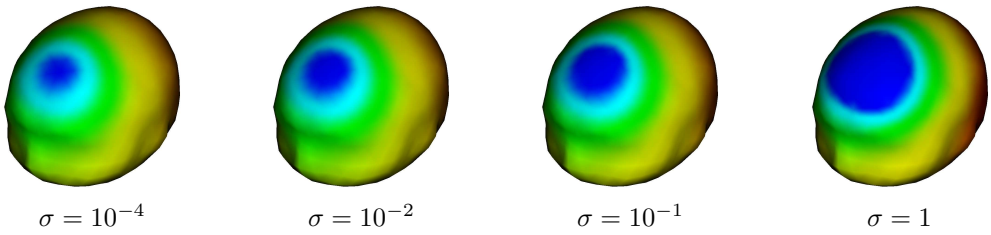

Figure 7. The surface potential for the realistic head models for different values of the hole compartment conductivity. The same colourmap was used for all images (red is positive, blue is negative). After mean subtraction.

with metal or with CSF) that creates a blurring effect. When the dipole is further away, the hole-induced changes are much smaller.

4. Conclusions

We have developed and implemented a variant of the symmetric BEM for models consisting of almost arbitrary partitioning of the space into constant conductivity regions. The use of such models in MEG/EEG is necessary if one desires to model precisely not only pathological features but also standard human anatomy. Our experiments indicate that the effects of the generalized geometry models cannot be approximated by standard layered models. The presented method offers new modelling possibilities, and promises greater accuracy for MEG/EEG forward and inverse problems. One must however bear in mind that the head model generation process is a difficult problem. Another issue to be addressed concerns the application of the BEM to very large meshes. A possible remedy is to use acceleration methods, such as the fast multipole method¶ [30].

¶ The fast multipole method (FMM) is a hierarchical method based on approximating far interactions with multipole spherical harmonics series expansions.

1. Appendix: Integral operators

We recall here the four integral operators involved in the symmetric BEM, as defined in [5, 7, 17].

$$\big(\mathcal{N}f\big)(\mathbf{r}) = \int_{\partial\Omega} \partial^2_{\mathbf{n},\mathbf{n}'} G(\mathbf{r}-\mathbf{r}') f(\mathbf{r}')\,\mathrm{d}s(\mathbf{r}') \qquad \big(\mathcal{D}f\big)(\mathbf{r}) = \int_{\partial\Omega} \partial_{\mathbf{n}'} G(\mathbf{r}-\mathbf{r}') f(\mathbf{r}')\,\mathrm{d}s(\mathbf{r}')$$

$$\big(\mathcal{D}^* f\big)(\mathbf{r}) = \int_{\partial\Omega} \partial_{\mathbf{n}} G(\mathbf{r}-\mathbf{r}') f(\mathbf{r}')\,\mathrm{d}s(\mathbf{r}') \qquad \big(\mathcal{S}f\big)(\mathbf{r}) = \int_{\partial\Omega} G(\mathbf{r}-\mathbf{r}') f(\mathbf{r}')\,\mathrm{d}s(\mathbf{r}')\ .$$

If we restrict $\mathbf{r}$ to be on a surface Γ and use the notation Θ for $\partial\Omega$, the above operators represent mappings from functions defined on Θ to functions defined on Γ. For example, for the operator $\mathcal{S}$ we have:

$$\big(\mathcal{S}_{\Gamma\,\Theta} f\big)(\mathbf{r}) = \int_{\Theta} G(\mathbf{r}-\mathbf{r}') f(\mathbf{r}')\,\mathrm{d}s(\mathbf{r}'), \quad \mathbf{r}\in\Gamma\ .$$

2. Appendix: Representation Theorem

The Boundary Element Method is based on the fundamental Representation Theorem [4, 5]. For details on its application to the EEG problem refer to [17].

Theorem 1 (Representation Theorem) *Let $\Omega \subseteq \mathbb{R}^3$ be a bounded open set with a regular boundary $\partial\Omega$. Let $u : (\mathbb{R}^3\backslash\partial\Omega) \to \mathbb{R}$ be a harmonic function ($\Delta u = 0$ in $\mathbb{R}^3\backslash\partial\Omega$), satisfying the condition $\mathscr{H}$:*

$$\left\{\begin{array}{ll} \lim\limits_{r\to\infty} r\,|u(\mathbf{r})| & <\infty \\ \lim\limits_{r\to\infty} r\dfrac{\partial u}{\partial r}(\mathbf{r}) & =0\ , \end{array}\right. lr$$

and denote $p(\mathbf{r}) \stackrel{def}{=} \partial_{\mathbf{n}} u(\mathbf{r})$. Then

$$\left\{\begin{array}{lcll} -p & = & +\mathcal{N}[u] - \mathcal{D}^*[p] & \text{for } \mathbf{r}\notin\partial\Omega \\ u & = & -\mathcal{D}[u] + \mathcal{S}[p] & \end{array}\right.$$

$$\left\{\begin{array}{lcll} -p^{\pm} & = & +\mathcal{N}[u] + \big(\pm\frac{\mathcal{I}}{2} - \mathcal{D}^*\big)[p] & \text{for } \mathbf{r}\in\partial\Omega \\ u^{\pm} & = & \big(\mp\frac{\mathcal{I}}{2} - \mathcal{D}\big)[u] + \mathcal{S}[p] & \end{array}\right.$$

where $\mathcal{I}$ denotes the identity operator over $\partial\Omega$.

Acknowledgments

The first author was sponsored by the Czech Ministry of Education under Project MSM6840770012. We are grateful to the reviewers for their helpful comments on the manuscript.

[1] J. Phillips, R. Leahy, J. Mosher, and B. Timsari, "Imaging neural activity using MEG and EEG," *IEEE Engineering in Medicine and Biology Magazine*, vol. 16, no. 3, pp. 34–42, 1997.

[2] J. Sarvas, "Basic mathematical and electromagnetic concepts of the biomagnetic inverse problem," *Phys. Med. Biol.*, vol. 32, no. 1, pp. 11–22, 1987.

[3] M. Hämäläinen, R. Hari, R. J. IImoniemi, J. Knuutila, and O. V. Lounasmaa, "Magnetoencephalography— theory, instrumentation, and applications to noninvasive studies of the working human brain," *Reviews of Modern Physics*, vol. 65, no. 2, pp. 413–497, Apr. 1993.

[4] M. Bonnet, *Equations intégrales et éléments de frontière*. CNRS Editions, Eyrolles, 1995.
[5] J.-C. Nédélec, *Acoustic and Electromagnetic Equations*. Springer Verlag, 2001.
[6] G. Adde, M. Clerc, O. Faugeras, R. Keriven, J. Kybic, and T. Papadopoulo, "Symmetric BEM formulation for the M/EEG forward problem," in *Information Processing in Medical Imaging*, ser. LNCS, C. Taylor and J. A. Noble, Eds., vol. 2732. Springer, July 2003, pp. 524–535.
[7] J. Kybic, M. Clerc, T. Abboud, O. Faugeras, R. Keriven, and T. Papadopoulo, "A common formalism for the integral formulations of the forward EEG problem," *IEEE Transactions on Medical Imaging*, vol. 24, no. 1, pp. 12–28, Jan. 2005.
[8] D. B. Geselowitz, "On bioelectric potentials in an homogeneous volume conductor," *Biophysics Journal*, vol. 7, pp. 1–11, 1967.
[9] C. G. Bénar and J. Gotman, "Modeling of post-surgical brain and skull defects in the EEG inverse problem with the boundary element method," *Clinical Neurophysiology*, no. 113, pp. 48–56, 2002.
[10] R. Oostenveld and T. F. Oostendorp, "Validating the boundary element method for forward and inverse EEG computations in the presence of a hole in the skull," *Human Brain Mapping*, no. 17, pp. 192–192, 2002.
[11] O. Faugeras, F. Clément, R. Deriche, R. Keriven, T. Papadopoulo, J. Roberts, T. Viéville, F. Devernay, J. Gomes, G. Hermosillo, P. Kornprobst, and D. Lingrand, "The inverse EEG and MEG problems: The adjoint space approach I: The continuous case," INRIA, Tech. Rep. 3673, May 1999. [Online]. Available: http://www.inria.fr/RRRT/RR-3673.html
[12] J. C. de Munck, "A linear discretization of the volume conductor boundary integral equation using analytically integrated elements," *IEEE Trans. Biomed. Eng.*, vol. 39, no. 9, pp. 986–990, Sept. 1992.
[13] J. C. Mosher, R. B. Leahy, and P. S. Lewis, "EEG and MEG: Forward solutions for inverse methods," *IEEE Transactions on Biomedical Engineering*, vol. 46, no. 3, pp. 245–259, Mar. 1999.
[14] N. G. Gencer and I. O. Tanzer, "Forward problem solution of electromagnetic source imaging using a new BEM formulation with high-order elements," *Phys. Med. Biol.*, vol. 44, no. 9, pp. 2275–2287, 1999.
[15] M. S. Hämäläinen and J. Sarvas, "Realistic conductivity geometry model of the human head for interpretation of neuromagnetic data," *IEEE Trans. Biomed. Eng.*, vol. 36, no. 2, pp. 165–171, Feb. 1989.
[16] Z. Akalm-Acar and N. G. Gençer, "An advanced boundary element method (BEM) implementation for the foward problem of electromagnetic source imaging," *Physics in Medicine and Biology*, no. 49, pp. 5011–5028, 2004.
[17] J. Kybic, M. Clerc, T. Abboud, O. Faugeras, R. Keriven, and T. Papadopoulo, "Integral formulations for the EEG problem," INRIA, Tech. Rep. 4735, Feb. 2003. [Online]. Available: http://www-sop.inria.fr/rapports/sophia/RR-4735.html
[18] J. Kybic and M. Clerc, "Symmetric BEM and multiscale fast multipole method for the E/MEG problem," in *NFSI 2003: Proceedings of the 4th International Symposium on Noninvasive Functional Source Imaging Within the Human Heart and Brain*, V. Pizzella and G. L. Romani, Eds., Berlin, Germany, Sept. 2003, pp. 122–124.
[19] D. R. Wilton, S. M. Rao, A. W. Glisson, D. H. Schaubert, O. M. Al-Bundak, and C. M. Butler, "Potential integrals for uniform and linear source distributions on polygonal and polyhedral domains," *IEEE Trans. Antenn. Propag.*, vol. 32, no. 3, pp. 276–281, Mar. 1984.
[20] A. S. Ferguson, X. Zhang, and G. Stroink, "A complete linear discretization for calculating the magnetic field using the boundary element method," *IEEE Trans. Biomed. Eng.*, vol. 41, no. 5, pp. 455–459, May 1994.
[21] J. N. Lyness and D. Jespersen, "Moderate degree symmetric quadrature rules for the triangle," *J. Inst. Maths Applics*, vol. 15, pp. 19–32, 1975.
[22] R. Cools, D. Laurie, and L. Pluym, "Algorithm 764: Cubpack++ — a C++ package for automatic two-dimensional cubature," *ACM Trans. Math. Software*, no. 23, pp. 1–15, 1997. [Online]. Available: http://www.cs.kuleuven.ac.be/~nines/research/CUBPACK/
[23] S. Tissari and J. Rahola, "Error analysis of a new Galerkin method to solve the forward problem in MEG and EEG using the boundary element method," CERFACS, Tech. Rep. TR/PA/98/39, 1998, toulouse, France.
[24] G. Fischer, B. Tilg, R. Modre, F. Hanser, B. Messnarz, and P. Wach, "On modeling the Wilson terminal in the Boundary and Finite Element Method," *IEEE Trans. Biomed. Eng.*, vol. 49, no. 3, pp. 217–224, Mar. 2002.
[25] M. Benzi, G. H. Golub, and J. Liesen, "Numerical solutions of saddle point problems," *Acta Numerica*, pp. 1–37, 2005.

[26] R. Barret, M. Berry, T. Chan, J. Demmel, J. Donato, J. Dongarra, V. Eijkhout, R. Pozo, C. Romine, and H. van der Vonst, *Templates for the Solution of Linear Systems: Building Blocks for Iterative Methods*. SIAM, 1994.

[27] C. Paige, B. Parlett, and H. Van der Vorst, "Approximate solutions and eigenvalue bounds from krylov subspaces," *Numerical Linear Algebra with Applications*, vol. 1, no. 1, pp. 1–7, 1993.

[28] A. Greenbaum, *Iterative methods for solving linear systems*, ser. Frontiers in Applied Mathematics. Society for Industrial and Applied Mathematics (SIAM), 1997, vol. 17.

[29] P. Tichý and J. Liesen, "Convergence analysis of krylov subspace methods," *GAMM Mitteilungen*, vol. 27, no. 2, 2004. [Online]. Available: http://www.math.tu-berlin.de/~tichy/download/public/LiTiGAMM2005.pdf

[30] J. Kybic, M. Clerc, O. Faugeras, R. Keriven, and T. Papadopoulo, "Fast multipole acceleration of the MEG/EEG boundary element method," *Physics in Medicine and Biology*, vol. 50, pp. 4695–4710, Oct. 2005.